Geophysical Prospecting

ORIGINAL ARTICLE OPEN ACCESS

Shear-Wave Splitting Measured for Permanent Reservoir Monitoring Systems: An Example From the Snorre Field

Joseph Asplet[1] | J-Michael Kendall[1] | Annie Jerkins[2] | Tom Kettley[1]

[1]Department of Earth Sciences, University of Oxford, Oxford, UK | [2]NORSAR, Kjeller, Norway

Correspondence: Joseph Asplet (joseph.asplet@earth.ox.ac.uk)

Received: 5 September 2025 | **Revised:** 20 March 2026 | **Accepted:** 6 April 2026

ABSTRACT

Microseismic monitoring of offshore CO_2 storage projects is likely to include some deployment of offshore sensors. To improve the value proposition of this monitoring infrastructure, it is important to consider what other information can be gained about the CO_2 storage complex and the surrounding region. Shear-wave splitting is one potential source of added value to microseismic monitoring of CO_2 storage operations at minimal additional cost, if factored in during network design. Shear-wave splitting provides a means to passively monitor the in situ horizontal maximum stress azimuth and potentially the magnitude of differential horizontal stresses. We demonstrate this for offshore monitoring of reservoirs using data recorded by the permanent reservoir monitoring network at the Snorre field. We measure shear-wave splitting for the M_W 5.1 Tampen Spur earthquake and subsequent microseismic aftershocks. Our results show that high-quality shear-wave splitting measurements can be made for microseismicity, with $M_L \geq 0.7$, recorded by seafloor instruments. At Snorre, the average shear-wave splitting fast polarisation direction $\phi_f = 92 \pm 15$ and percentage anisotropy $\xi = 2.68 \pm 0.26$. This is consistent with microcracks preferentially aligned with the maximum horizontal stress azimuth. At Snorre, we estimate this as 108 ± 4 using data from the World Stress Map. The shear-wave splitting results contain two groups of fast polarisation directions. The four westernmost stations cluster around $\phi_f = 68 \pm 13$ with the remaining clustering around $\phi_f = 113 \pm 4$. This variation may be due to the depletion history of the reservoir. Incorporating shear-wave splitting into microseismic monitoring plans potentially allows for semi-continuous measurements of the changes to the stress field in the storage complex and surrounding region, provided there is sufficient microseismicity. This demonstrates that shear-wave splitting is a valuable dataset for monitoring the offshore subsurface stress field, which should be considered when planning offshore passive seismic monitoring.

1 | Introduction

Geological CO_2 storage is an essential part of global net-zero strategies. Many countries including the United Kingdom, Norway, Denmark and the Netherlands are developing offshore geological storage projects in the North Sea, as the geology is favourable for geological storage and there is existing infrastructure and technical expertise which can be redeployed (Furre et al. 2019; Skurtveit et al. 2022). With the growth in project development, there is an increasing demand for new approaches to characterise the in situ stress state of prospective sites and to monitor the geomechanical response of the storage complex to CO_2 injection. This is needed to ensure the safety and operability of CO_2 storage sites (Skurtveit et al. 2022).

One important component of monitoring geological carbon storage projects is seismicity. Fluid injection has been associated with seismicity in a wide range of geological settings (e.g., Keranen and Weingarten 2018) including CO_2 injection (e.g., Stork et al. 2015; Harvey et al. 2021; Bauer et al. 2022) and offshore gas storage (Cesca et al. 2014). For the North Sea, a high-quality seismicity catalogue has been compiled (Kettley et al. 2024),

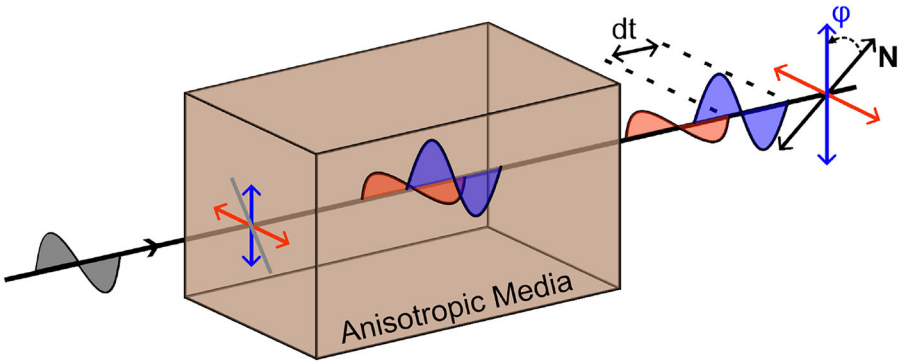

Figure 1 | Schematic cartoon illustrating shear-wave splitting.

enabling improved assessment of faulting, the background stress field, leakage risk, and seismic hazard for projects (e.g., Larsen et al. 2024, Kühn et al. 2024). One recommendation from this body of work is that offshore seismic monitoring infrastructure is needed if seismicity near CO_2 storage projects is to be monitored with sufficient accuracy. Offshore (i.e., near-source) observations are vital in calculating accurate earthquake locations (particularly depths), focal mechanisms and magnitudes.

Achieving a high-quality catalogue of seismicity is the primary product for any passive seismic monitoring programme, to better understand how the reservoir is responding to injection. However, deploying networks of seismometers on the seafloor has the potential to generate highly valuable secondary datasets, further aiding that understanding, particularly if acquiring these secondary data products is incorporated into the network design. One such dataset is shear-wave splitting, which is an indicator of seismic velocity anisotropy – the variation in seismic velocity with propagation direction – measured using microseismicity. This can provide a measure of the in situ stress field. Fracture-induced seismic anisotropy has previously been observed using four-component sea-bottom cable systems at the Valhall field using P wave amplitude variation with offset and azimuth (AVOA; Hall and Kendall 2003) and seismic interferometry (Mordret et al. 2013). Such seafloor instrumentation has been previously used to monitor induced seismicity (Chambers et al. 2010)

1.1 | Shear-Wave Splitting

Shear-wave splitting, or seismic birefringence, occurs when a shear-wave propagates through an anisotropic medium. The incident shear-wave is split into two sub-perpendicular shear-waves, which propagate through the medium at different velocities (Figure 1). The polarisation of the fast shear-wave (ϕ) and the delay time between the split shear waves (δt) are measured, where ϕ is related to the orientation of the symmetry axes of the anisotropic medium and δt to the strength of the anisotropy. Shear-wave splitting is typically measured using passive seismic data and has been measured in many industrial settings using microseismic data (e.g., Al-Harrasi, Kendall, et al. 2011; Stork et al. 2015; Hudson et al. 2024, etc.) including for offshore fields using data from borehole geophones (Valhall; Teanby, Kendall, Jones, et al. 2004) and ocean bottom instruments (Ekofisk; Jones et al. 2014).

In the Earth, there are many potential mechanisms for seismic anisotropy. At the reservoir scale and depth, the predominant mechanism is preferential alignment of near-vertical micro-scale fractures with the azimuth of maximum horizontal stress (SHmax; Nur and Simmons 1969; Crampin 1987; Zatsepin and Crampin 1997). This mechanism produces a hexagonal anisotropy with a horizontal symmetry axis, known as horizontal transverse isotropy (HTI). Sedimentary strata can also develop anisotropy either through periodic layering of different units (e.g., Backus 1962) or preferred alignment of anisotropic minerals such as phylosilicates (J.-M. Kendall et al. 2007). These mechanisms, however, produce a hexagonal anisotropy with a vertical symmetry axis or vertical transverse isotropy (VTI). In passive seismic studies where receivers are at the surface, the incident shear-waves are near vertical and, therefore, are not sensitive to VTI. If data from borehole geophones are used, where ray-paths are propagating horizontally from sources to receivers, then this contribution from sedimentary fabrics, and the fact that the combination of VTI and HTI mechanisms produces an anisotropy with an orthorhombic symmetry, must be considered but can provide additional reservoir information (Baird et al. 2013). Where the observed seismic anisotropy is due to the stress-induced alignment of micro-scale fractures, this can be used to gain information on the in situ stress field, particularly the orientation of maximum horizontal stress (S_{Hmax}). S_{Hmax} is generally parallel to fracture strike and, therefore, to the shear-wave splitting fast polarisation direction. This allows for the orientation of S_{Hmax} to be interpreted from passive seismic shear-wave splitting datasets (e.g., Savage et al. 2010; Igonin et al. 2022; Guzman et al. 2022; Hudson et al. 2024). In some cases, it has been possible to infer changes in the stress state at a reservoir using temporal variations in shear-wave splitting (e.g., Teanby, Kendall, Jones, et al. 2004; Stork et al. 2015) and in tectonic (e.g., Pastori et al. 2019) and volcanic settings (e.g., Gerst and Savage 2004; J.-M. Kendall et al. 2025). The Ekofisk Microseismic experiment, where microseismic data were acquired over an 18-day period in April 1997 at the Ekofisk oil field in the North Sea, showed that shear-wave splitting could be used to illuminate spatial variations in aseismic fracture sets (Jones et al. 2014).

Whilst shear-wave splitting has been measured for microseismicity in offshore settings, such as at Valhall (Teanby, Kendall, Jones, et al. 2004) and Ekofisk (Jones et al. 2014), this has relied on geophones installed in monitoring boreholes. Using seafloor instrumentation, such as ocean bottom seismometers or perma-

nent reservoir monitoring deployments, to measure shear-wave splitting has proved challenging given the increased noise levels in the marine environment and uncertainty on sensor component orientations. Where shear-wave splitting has been measured using seafloor instruments, it has often been for teleseismic shear-wave in deeper oceanic environments (e.g., Harmon et al. 2004; Collins et al. 2012; Scholz et al. 2018). Shear-wave splitting has been successfully measured for earthquakes with $M \geq 2.5$ using a deployment of 150 ocean bottom seismometers over a subsea area of 300×1000 km off the coast of northeastern Japan (S-net; Uchida et al. 2020).

The potential application to CO_2 storage is particularly exciting, since ensuring safe and reliable geological CO_2 storage requires new methods to monitor the geomechanical response of reservoirs to injection (Skurtveit et al. 2022). This is because the in situ stress state can naturally have a significant impact on the operation and containment risk assessment of storage projects. Many potential CO_2 storage sites require drilling and operating injection wells in regions or depths that may not have had previous hydrocarbon exploration, and, therefore, there may be fewer data to conduct leakage risk assessments. Additional means of constraining stress or fracturing are valuable, particularly when they are derived from independent geophysical methods, to image the reservoir, seal and overburden units. Fracture and fault trends in particular are important inputs in containment risk assessment, as their orientations with respect to in situ stresses significantly affect their potential behaviour when stress changes occur as a result of injection. The likelihood of fault failure, fracture development and other deformation is affected by stress, and thus it is a critical variable to constrain when assessing a field for CO_2 injection and monitoring operations.

Understanding the in situ stress state can have a significant impact on the operation and containment risk assessments of storage projects. Many potential CO_2 storage sites require drilling and operating injection wells in regions or depths that may not have had previous hydrocarbon exploration, and, therefore, there may be fewer data to conduct leakage risk assessments. Additional means of constraining stress or fracturing are valuable, particularly independent geophysical methods to image the reservoir, seal and overburden units. Fracture and fault trends in particular are important inputs in containment risk assessment, as their orientations with respect to in situ stresses significantly affect their potential behaviour when stress changes occur as a result of injection. The likelihood of fault failure, fracture development and other deformation is affected by stress, and thus it is a critical variable to constrain when assessing a field for CO_2 injection and monitoring operations.

2 | Data

2.1 | Permanent Reservoir Monitoring Systems

Permanent reservoir monitoring (PRM) systems, consisting of three-component geophones and hydrophones, have been deployed to monitor oil and gas fields in the northern North Sea (Thompson et al. 2015). Similar PRM systems could be an option for monitoring of offshore CO_2 storage fields, but shear-wave splitting is not routinely measured for data recorded by these systems. PRM data for three fields in the northern North Sea – Snorre, Grane and Oseberg – are good sites to test the potential for PRM systems to measure shear-wave splitting. Data from select PRM stations are shared with the Norwegian National Seismic Network (NNSN; Figure 3; Ottemöller et al. 2021). The PRM systems installed at the Snorre field are the only ones found to have suitable seismicity, using the unified North Sea earthquake catalogue produced by the SHARP project (Kettley et al. 2024;;2025). The PRM system installed at Snorre is one of the largest in the world (Thompson et al. 2015; Jerkins et al. 2024), consisting of a seismic cable containing 10,708 four-component sensors, which have an eigenfrequency of 15 Hz. To mitigate the impact of sensor noise at 15 Hz, all waveform data are zero-phase bandpass filtered between 1 and 10 Hz.

Whether shear-wave splitting can be measured for an earthquake is limited by the 'shear-wave window'. Interactions with the free surface affect the particle motion of shallow incident angle shear-waves (Nuttli 1961). To avoid these effects, shear-wave splitting is only measured where the incidence angle is less than the critical angle (Booth and Crampin 1985). We use a critical angle, or shear-wave window, of 45° for straight-line ray paths between the source and receiver. This assumes that low-velocity layers near the surface will turn incident shear-wave ray paths such that they are near-vertical at the free surface.

These events include the 21st March 2022 M_W 5.1 Tampen Spur earthquake and 26 subsequent aftershocks. The mainshock and five subsequent aftershocks are taken from the unified North Sea earthquake bulletin (Kettley et al. 2024;;2025). This initial dataset is supplemented by additional aftershocks detected using the Snorre PRM system (Jerkins et al. 2024). The aftershocks have local magnitudes in the range $-0.6 < M_L < 2.6$. Waveform data for all earthquakes were obtained for the 10 PRM nodes shared with the NNSN, and for the Tampen Spur mainshock data from an additional 50 PRM stations were provided by Equinor. An example of the data used, which includes horizontal component seismograms recorded by PRM stations within the shear-wave window of an M_L 0.7 aftershock, is shown in Figure 2.

2.2 | Stress Data

Data from the 2025 release of the World Stress Map (Heidbach et al. 2025) are used to characterise the regional S_{Hmax} azimuth near the Snorre field (Figure 3). This dataset comprises 129 data points across the northern North Sea compiled from a variety of measurement types including earthquake focal mechanisms (24 data points), borehole breakouts (58 data points), overcoring (five data points), and drilling-induced tensile fractures (24 data points). Data in the World Stress Map are assigned a data quality code based on their reliability to assess regional stress field orientation (Heidbach et al. 2016). Only data which are rated as A, B, or C on the World Stress Map data quality scheme are used, which gives a stress dataset comprising 50 measurements. The quality codes A, B and C indicate that the data have an uncertainty in S_{Hmax} orientation of ±15°, ±20° or ±25°, respectively.

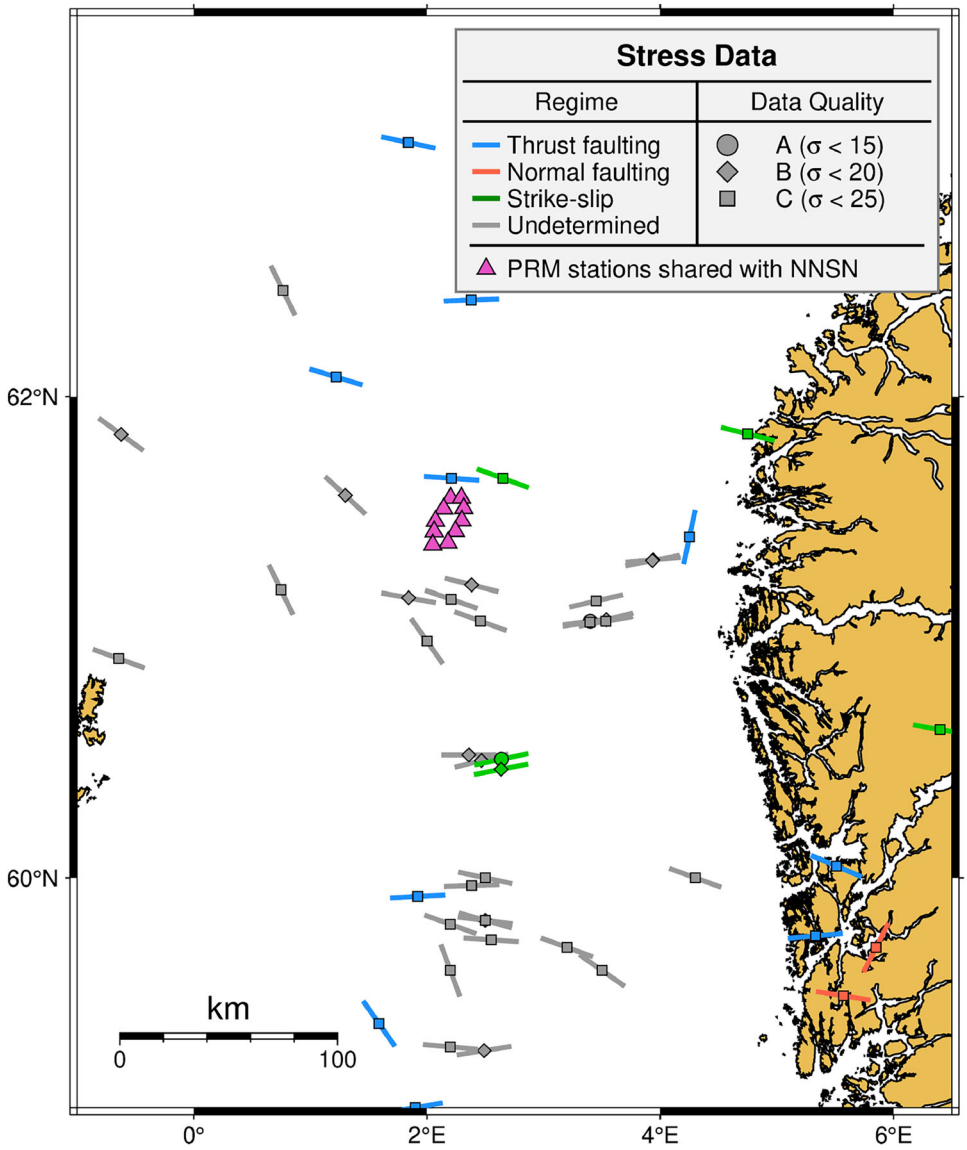

Figure 3 | Map showing borehole stress data from the World Stress Map database (Heidbach et al. 2025). Bars show the interpreted S_{Hmax} orientation and symbols correspond to data quality, where A (circle) has an uncertainty in S_{Hmax} orientation of < 15, B (diamond) has an uncertainty of < 20 and C (square) has an uncertainty of < 25. Magenta triangles show the location of Snorre PRM stations that share data with the NNSN.

3 | Method

If a shear-wave has only propagated through isotropic media, and has a sufficiently vertical incidence angle such that phase shifts from interactions with the free surface can be neglected (Nuttli 1961), the displacement recorded by a single seismometer can be written as:

$$\mathbf{u}(\boldsymbol{\omega}) = u(\omega)\hat{\mathbf{p}} \tag{1}$$

in the frequency domain, where $u(\omega)$ is the source wavelet in the frequency domain and $\hat{\mathbf{p}}$ is the source polarisation. In this case, the expected particle motion in the horizontal components is linear. If, however, the shear-wave propagates through anisotropic media, the delay time added by shear-wave splitting results in a phase shift which produces a characteristic elliptical particle motion. Therefore, shear-wave splitting can be effectively measured by searching for a set of shear-wave splitting parameters $(\phi, \delta t)$ which restore a linear particle motion. Here, a method known as eigenvalue minimisation is used to characterise particle motion linearity (Silver and Chan 1991; Walsh et al. 2013a). For a shear-wave isolated in a time window of interest, where the optimum time window is found using cluster analysis (Teanby, Kendall, and Van der Baan 2004), the horizontal component seismograms are rotated from the geographic to the radial-transverse reference frame, and the covariance matrix is computed following Walsh et al. (2013a). The first and second eigenvalues, λ_1 and λ_2, correspond to the energy of the radial and transverse components, respectively. Using the implementation of Wuestefeld et al. (2010), we grid search over the range of plausible shear-wave splitting parameters, $-90 \leq \phi_f \leq 90$ and $0\,\text{s} \leq \delta t \leq 0.1\,\text{s}$, seeking to minimise $\frac{\lambda_2}{\lambda_1}$. Error estimates in $\phi_f, \delta t$ are made using a 95% confidence region defined by

$$\lambda_2(\phi_f, \delta_t) \leq \lambda_{2_{min}}\{1 + [k/(\upsilon - k)]F^{0.05}_{k,\upsilon-k}\}, \tag{2}$$

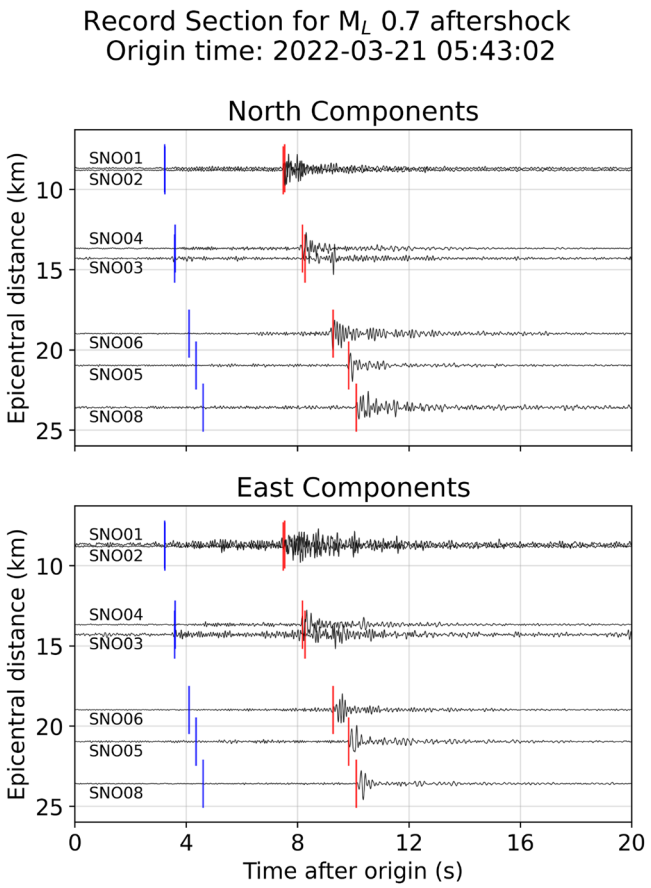

Figure 2 | Horizontal component seismograms recorded by permanent reservoir monitoring stations for an M_L 0.7 aftershock of the M_W 21st March 2022 Tampen Spur earthquake. Blue and red bars show the P and S arrival times reported in the NNSN Bulletin (Norwegian National Seismic Network (NNSN) 2025). Only data for PRM sensors within the shear-wave window of the event are shown. Waveforms are zero-phase bandpass filtered between 1 and 10 Hz.

where k is the number of parameters, in this case 2, υ is the estimated degrees of freedom of the data and $F_{k,\upsilon-k}$ is an F-distribution (Silver and Chan 1991; Walsh et al. 2013a). Standard errors in $\phi_f, \delta t$ are then estimated by taking the quarter of the length and width of the 95% uncertainty ellipsoid. Figure 4 shows an example shear-wave splitting measurement made for an M_L 0.7 aftershock of the Tampen Spur event. This example has a signal-to-noise ratio of 5.

All measurements are manually inspected to ensure clear shear-wave splitting has been observed. Input waveforms, selected shear-wave measurement windows, corrected waveforms and eigenvalue minimisation surface (Figure 4) are inspected to ensure a good shear-wave splitting measurement has been made. Only measurements with $\sigma_{\phi_f} \leq 25$ and $\sigma_{\delta t} \leq 0.015$ s, with clearly linearised corrected particle motions (Figure 4), are used and considered to be good quality and used for subsequent analysis. This inspection process is important as crustal shear-wave splitting measurements commonly suffer from cycle skipping, and other free surface effects which can distort measured fast polarisations (e.g., Matcham et al. 2000; Walsh et al. 2013b).

The measured shear-wave splitting delay time, δt, is integrated along the entire ray path. Therefore, δt may vary with earthquake depth depending on the thickness of the anisotropic medium. To correct for ray path length effects, δt is converted to per cent anisotropy,

$$\xi = 100(V_S * \frac{\delta t}{d}), \tag{3}$$

where V_S is an assumed mean shear-wave velocity and d is the ray path length, assuming a straight ray from source to receiver.

4 | Results

Shear-wave splitting measurements are made using waveform data for the Tampen Spur mainshock and subsequent aftershocks recorded by permanent reservoir monitoring stations at Snorre. After discounting stations that are outside of the shear-wave window for the earthquakes, we are able to make 124 shear-wave splitting measurements. After data quality control, there are 26 good quality measurements of shear-wave splitting, with a further 28 clear null measurements where no shear-wave splitting is observed. Figure 5 shows the 26 good quality shear-wave splitting measurements at the recording station. The level of data attrition, with approximately 21% of measurements resulting in good quality splits, is low but within the normal range of what is achieved for land-based studies of shear-wave splitting (e.g., Stork et al. 2015; Nowacki et al. 2018; Asplet et al. 2024; M. Kendall et al. 2025; Asplet et al. 2025). One reason for data attrition here is that few of the PRM sensors yield usable shear-wave splitting measurements for the Tampen Spur mainshock. This is due to the larger amplitude shear-waves either not being fully recorded due to data clipping, or the energetic wave trains cause significant ringing on the sensors. Both mean that clear shear-wave splitting measurements cannot be made. Figure 6 shows the S-phase recorded by the closest line of 10 PRM sensors to the mainshock. No good quality shear-wave splitting measurements can be made for these data.

To estimate the regional S_{Hmax} azimuth at Snorre, we use data from the 2025 release of the World Stress Map (Heidbach et al. 2025). However, there are few datapoints close to Snorre, with the closest being 19 km from the centre of the PRM network. The regional S_{Hmax} azimuth is estimated by taking the circular mean of the 25 datapoints that are within 50 km of the centre of the PRM network. This gives a regional S_{Hmax} of 108 ± 4. This estimate of S_{Hmax} rotates to favour a near east-west S_{Hmax} azimuth as the radius of the averaging area increases (Figure 7).

The good quality shear-wave splitting measurements are concentrated in the North of the Snorre field (Figure 5). Seven measurements of shear-wave splitting are made for the Tampen Spur mainshock, with the remaining 19 made for the aftershocks. Of those, 12 are made for aftershocks with $M_L \leq 1.0$. Averaging the ϕ_f results from all the PRM sensors gives a circular mean ϕ_f of -87 ± 14 (Figure 8). When aggregated, the ϕ_f measurements show a slight bimodal distribution. This arises as the measured ϕ_f varies across the stations, with stations SNO01, SNO03, SNO05 and SNO08 measuring ϕ_f approximately oriented northeast-southwest (Figures 5 and 9a). The 13 ϕ_f measurements made for

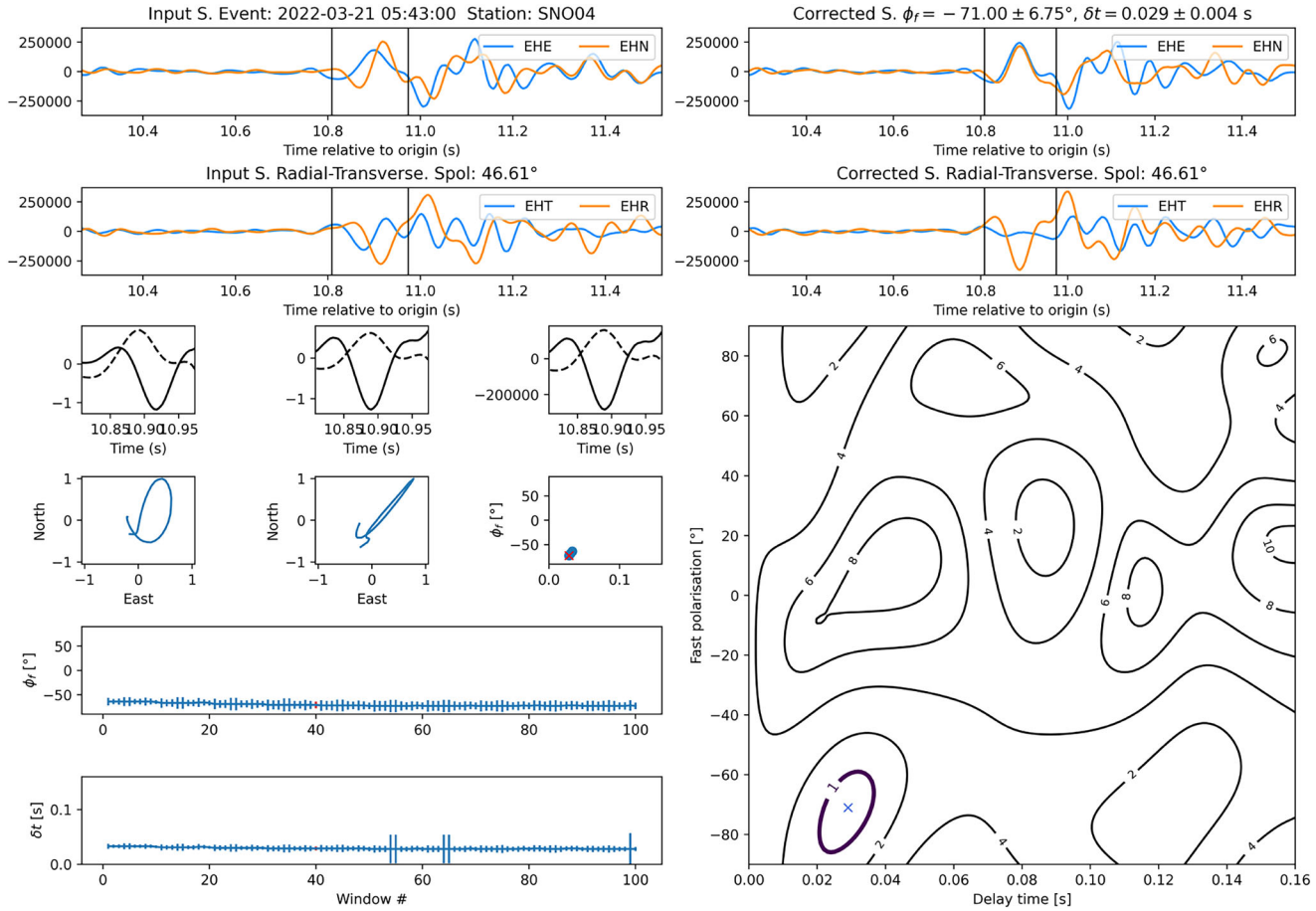

Figure 4 | Example shear-wave splitting measurement made at for an M_L 0.7 earthquake, which occurred at 21 March 2022, 05:41:43 UTC and was recorded by PRM sensor SNO04 at the Snorre field. After manual inspection, this measurement is categorised as an 'A' or high-quality measurement of shear-wave splitting. The top panels show the input (top left) and corrected (top right) shear-wave phase, where the vertical black bars show the optimum analysis window. Waveforms are zero-phase bandpass filtered between 1 and 10 Hz. The second row shows the input and corrected waveforms rotated to the measured source polarisation direction. The third row shows the normalised input and corrected waveforms, along with the unnormalised, corrected waveforms. The fourth row shows particle motion plots, which show the North and East component waveforms plotted against each other, for the input and corrected waveforms, along with the measured fast polarisation (ϕ_f) and delay time (δt) for each window used in the cluster analysis of Teanby, Kendall, and Van der Baan (2004). Lower panels show ϕ_f and δt plotted against the window number. The contour plot on the lower right shows the summarised result of the grid search over $\phi_f, \delta t$ for the optimum analysis window, with contours showing the objective function $\frac{\lambda_2}{\lambda_1}$. Here, $\frac{\lambda_2}{\lambda_1}$ has been normalised by the estimated 95% confidence value (Equation 2) with the bold contour enclosing the 95% confidence region. Blue cross shows the best fitting shear-wave splitting parameters.

data recorded by SNO01, SNO03, SNO05 and SNO08 (hereafter referred to as Group 1) have a circular mean of $\bar{\phi_f} = 68 \pm 13$, and the circular mean for the 12 ϕ_f measurements made at the remaining stations (or Group 2) is -64 ± 6 (Figure 9).

Shear-wave splitting delay times are converted to ξ following Equation (3). As all the earthquakes used here have focal depths in the range of 19.5-26.2 km (Jerkins et al. 2024), the measured δt are small relative to the ray path lengths with a mean ξ of 1.07 ± 0.08, assuming a mean V_S of 5.7 km s^{-1}, calculated from a one-dimensional velocity model for the region (Jerkins et al. 2024). As we expect, the majority of the anisotropy to be concentrated in the upper 5 km, we also calculate ξ using this assumption, fixing the ray path length to 5 km and using an average V_S of 2.8 km s^{-1}. Under this assumption, the mean ξ is 2.61 $\pm$ 0.25. Figure 10 shows histograms of ξ for all shear-wave splitting measurements.

5 | Discussion

The results show that shear-wave splitting can be measured for microseismicity recorded by seafloor permanent reservoir monitoring systems. This demonstrates that projects with nearby seafloor passive seismic sensors could use shear-wave splitting as a valuable tool for monitoring in situ S_{Hmax} azimuth at a higher spatial resolution than can be practicably achieved with stress data derived from borehole data. The percentage anisotropy results suggest that, as expected, the shear-wave splitting is mainly sensitive to anisotropy due to aligned microcracks in the upper crust. When we assume this region is 5km thick, $\bar{\xi} = 2.61 \pm 0.25$, which is in line with what would be expected for anisotropy due to aligned microcracks in the uppermost crust (e.g., Teanby, Kendall, Jones, et al. 2004; Al-Harrasi, Al-Anboori, et al. 2011). The ϕ_f results show a clear bimodal pattern (Figure 8a). This is

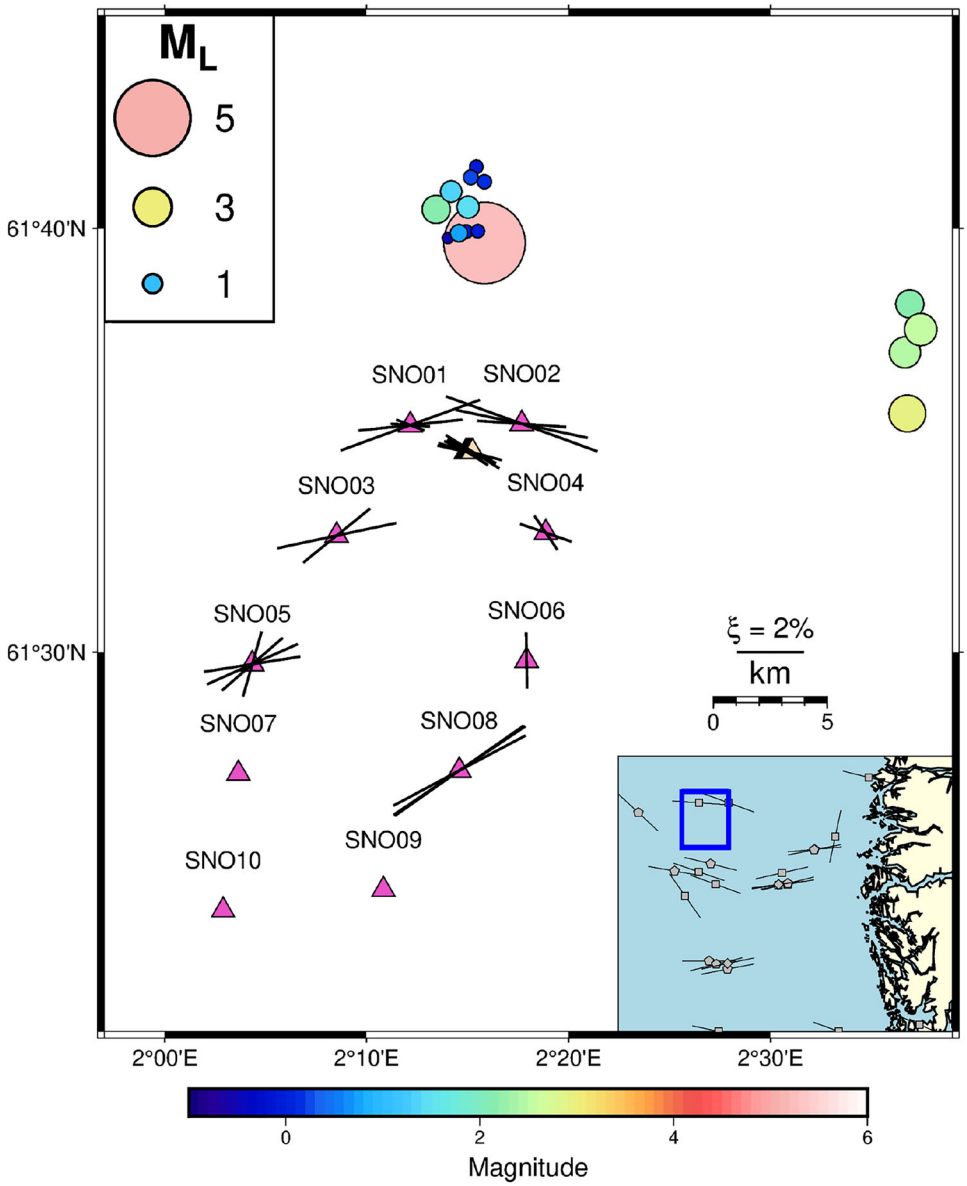

Figure 5 | Shear-wave splitting measurements for data from PRM stations (triangles) at the Snorre field. Shear-wave splitting measurements are shown by the black bars whose orientation corresponds to ϕ, and the length is proportional to ξ, which is calculated from δt following Equation (3) assuming a V_S of 2.8 km s^{-1} and a 5-km thick layer of anisotropy. Earthquakes used (coloured by magnitude), the 21$_{st}$ March 2022 M$_W$ 5.1 Tampen Spur earthquake and subsequent aftershocks, are plotted at the locations of Jerkins et al. (2024). Earthquakes located to the East of Snorre were not included in the relocation study, with locations instead taken from the unified North Sea catalogue (Kettlety et al. 2025). Data from 10 PRM stations (SNO01–SNO10), which are shared with the Norwegian National Seismic Network (magenta circles Ottemöller et al. 2021), are used for all earthquakes. For the Tampen Spur mainshock, waveform data from an additional 50 PRM stations were provided by Equinor (pale yellow triangles). The inset map shows borehole stress data taken from the World Stress Map database (Heidbach et al. 2025), plotted as in Figure 3.

due to spatial variability in the data, with ϕ_f data for the Group 2 stations (circular mean -64 ± 6; Figure 9b) strongly agreeing with regional S_{Hmax} azimuth (108 ± 4; Figure 8b). The ϕ_f results for Group 1 form a second cluster rotated by 45° from the Group 2 results. This could represent a 45° rotation in the local S_{Hmax} azimuth at these southern and western stations. Similar-scale local-scale variations in ϕ_f have been observed by local studies of shear-wave splitting for microseismicity near a geothermal project and interpreted as local rotation of the S_{Hmax} azimuth (Hudson et al. 2024). Reservoir-scale rotations of microscale fracture strike were observed for the Valhall field from amplitude variation with offset and azimuth (AVOA Hall and Kendall 2003) and seismic interferometry (Mordret et al. 2013). Spatial and temporal variations in shear-wave splitting were also observed using downhole microseismic monitoring, with reservoir-scale rotations in ϕ_f of up to 90° (Teanby, Kendall, Jones, et al. 2004). At Valhall, the elliptical pattern in seismic anisotropy is associated with a radial S_{Hmax} azimuth tangential to a production-related subsidence bowl (Hatchell et al. 2009; Herwanger and Horne 2009; Mordret et al. 2013). The temporal variations in seismic anisotropy have been since been explained as a cyclic recharge and dissipation of cap-rock stresses in response to production-

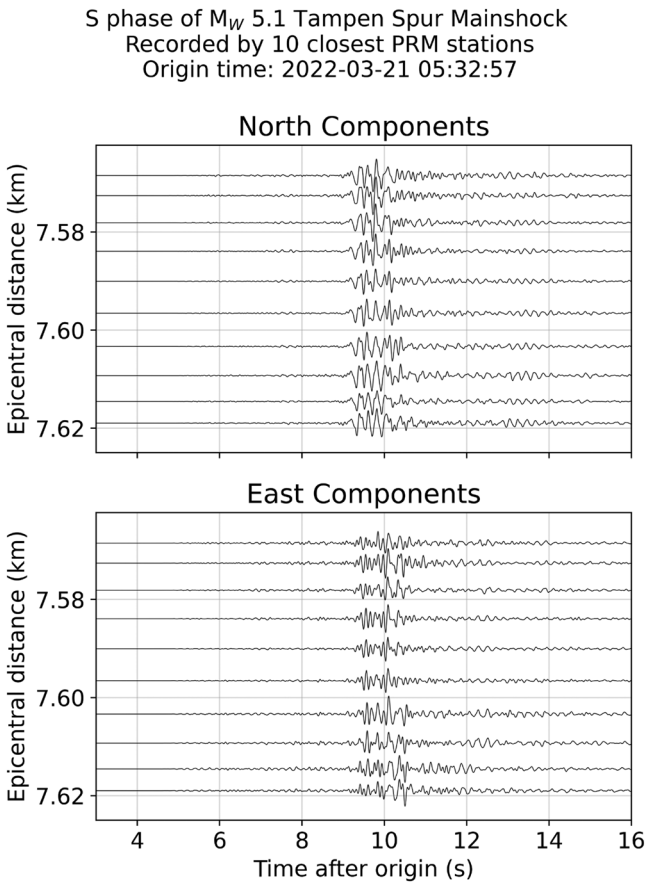

Figure 6 | Horizontal component seismograms showing the shear-wave arrivals from the M_W 21st March 2022 Tampen Spur earthquake recorded by the 10 PRM sensors closest to the hypocenter that were available to this study. Waveforms are zero-phase bandpass filtered between 1 and 10 Hz.

driven compaction of the underlying oil reservoir (De Meersman et al. 2009).

One important difference between the data used in this study and the anisotropy studied at Valhall is that the seismicity has depths in the range of 19.5-26.2 km (Jerkins et al. 2024), and that, therefore, the shear-wave splitting and interpreted S_{Hmax} corresponds to the stress field averaged across the upper ca. 5 km of crust and not the state of stress within the Snorre field or overlying formations. Whilst the rotation in ϕ_f at Snorre may be associated with the depletion history of the reservoir, with the data available, other explanations cannot be ruled out. One plausible alternate explanation is a more complicated anisotropic fabric, perhaps due to multiple cross-cutting fracture sets (e.g., Al-Harrasi, Al-Anboori, et al. 2011; Verdon and Kendall 2011). For this study, it was only possible to use data from a handful of PRM stations at Snorre, and analysis data from all 10,708 PRM sensors would allow for more detailed analysis as to whether this rotation in ϕ_f represents a local rotation in S_{Hmax} across the area.

Shear-wave splitting has been previously measured using microseismicity at reservoir depths using both downhole (Teanby, Kendall, Jones, et al. 2004) and seafloor instruments (e.g., Jones et al. 2014). Our results demonstrate that shear-wave splitting can also be routinely measured using naturally occurring microseismicity using offshore seafloor monitoring systems. Shear-wave splitting represents a valuable secondary dataset for a monitoring program, measured after microseismicity has been detected and located, which can be used to passively infer the in situ stress field. Prior to using shear-wave splitting for monitoring, it is important to characterise the stress state of the reservoir and the surrounding region prior to injection. This will allow existing local variations in seismic anisotropy, such as those observed here for Snorre and previously at Valhall (Hall and Kendall 2003; Teanby, Kendall, Jones, et al. 2004), to be characterised in advance. There are many factors, such as the stress sensitivity of rock units in the storage complex, the volumes and rate of injection, which could produce local changes in shear-wave splitting following injection.

Whilst deploying a PRM system at the same scale as that at Snorre may be unfeasible for typical CO_2 storage projects, the results for the 10 sensors shared with the NNSN (magenta triangles, Figure 5) yield a significant (15 out of 25) proportion of the shear-wave splitting dataset. Removing the 10 measurements made using an additional 50 sensors for the Tampen Spur mainshock does not change the interpretation of the results. This shows that even a minimal seafloor deployment could be used to measure microseismic shear-wave splitting for stress field monitoring.

To maximise the value shear-wave splitting can add to a monitoring network, it is important to consider the limitations of the technique, particularly the spatial limitations of the shear-wave window effect. For this study, we are fortunate that the 2022 Tampen Spur mainshock and subsequent aftershocks were sufficiently deep, in the range of 19.5-26.2 km (Jerkins et al. 2024) and close to the Snorre field that, with the exception of stations SNO7, SNO9 and SNO10, the PRM system was within the shear-wave window of natural seismicity. This limits the impact on data availability due to the shear-wave window effect (Nuttli 1961). To make use of data from potential induced microseismicity, which may have depths on the order of ca. 1 km depending on the depth of the reservoir, sensors would have to be more densely spaced or placed closer to the microseismic events. Where measurements are made, the shear-wave waveforms are clear and measurements can be made for multiple earthquakes with $M_L < 1.0$.

When measuring shear-wave splitting, it is important to consider the deployment of the sensors used and how this may affect the recorded signal. The PRM system at Snorre was initially installed in an open trench, approximately 0.5–1.5 m deep (Thompson et al. 2015; Gawron et al. 2025). Over time, this trench was infilled with soft sediment and mud, burying the PRM sensors. This trench infill can produce a downgoing 'trench ghost' shear-wave at the sensors due to the reflection of upgoing shear-waves at the seabed (e.g., Dawson et al. 2016). Trench ghosts have been observed, for frequencies as low as 8 Hz in certain locations, at Snorre, which suggests extremely low shear-wave velocity trench fill of less than 20 m s^{-1} (Gawron et al. 2025). This gives a travel time differential between direct S and the trench ghost in the range of 0.05–0.15 s for a vertically incident shear-wave, compared to the mean shear-wave splitting delay time of 0.047 ± 0.023 s. Therefore, it is plausible that trench ghosting could occur within the 1–10 Hz band used here and affect measured fast polarisation directions. However, given the low-velocity sediments near the surface, incident shear-waves will be near vertical. Therefore, we

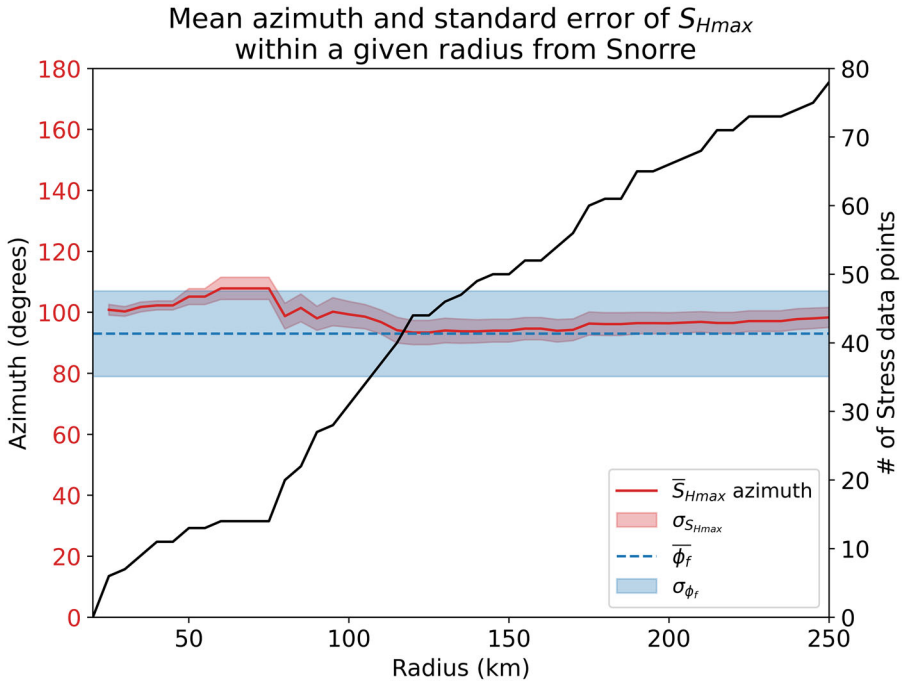

Figure 7 | Regional S_{Hmax} azimuth for Snorre (red line), estimated by taking the circular mean of S_{Hmax} azimuth data within a given radius of the centre of the PRM network, as a function of averaging radius compared to the circular mean ϕ_f (blue dashed line). The shaded regions show the circular standard errors. The black line shows the number of data points included in the averaging. S_{Hmax} azimuth data are taken from the 2025 version of the World Stress Map (Heidbach et al. 2025).

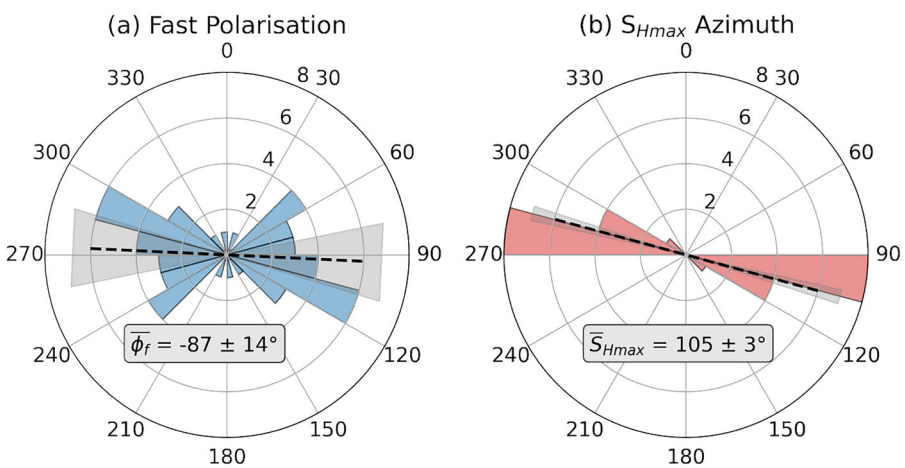

Figure 8 | Rose histograms showing the shear-wave splitting fast polarisation data at Snorre (a) and S_{Hmax} azimuth data within 50 km of Snorre (b). The black dashed line indicates the circular mean of each dataset, with the grey-shaded region representing the circular standard error. Individual shear-wave splitting measurements can be seen in Figure 5.

would expect the seabed reflection to have little effect on shear-wave polarisation, although the trench ghost would be phase shifted by 180°.

In this study, all measurements were inspected for data quality assurance. Only measurements for which the incoming shear waves are clear, the initial particle motion is elliptical, the corrected particle motion is well linearised and the results are stable over a range of measurement windows are used. This data inspection ensures that the shear-wave splitting measurements shown here (Figure 5) have no interference from trench-ghosting. Furthermore, there is no correlation between backazimuth and fast polarisation, which would evidence a phase conversion affecting measured shear-wave splitting. For routine monitoring, however, the effect of trench-ghosting on the vector fidelity of shear-wave splitting would require further study. The likely lower magnitude of events will require splitting to also be measured in higher frequency bands, where trench ghosting is more likely. Monitoring shear-wave splitting alongside microseismic monitoring for a full 10,000 sensor PRM system would make

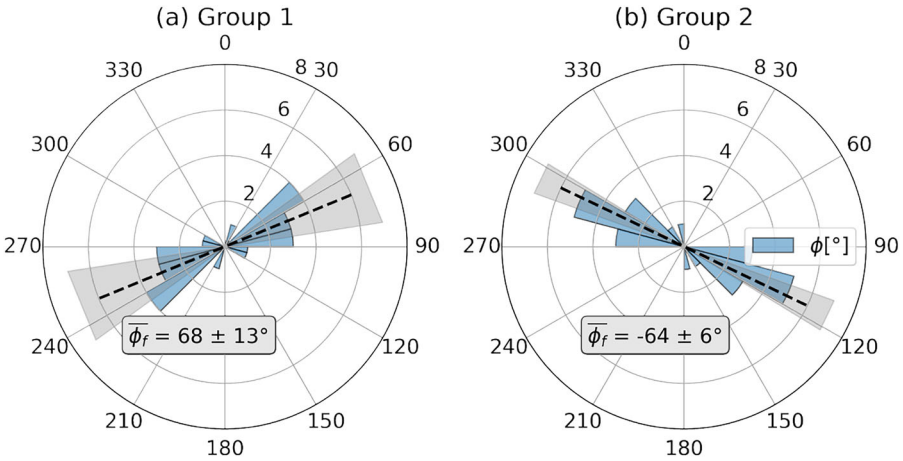

Figure 9 | Rose histograms showing the shear-wave splitting fast polarisation data at Snorre recorded by the PRM stations SNO01, SNO03, SNO05 and SNO08 (a) and the remaining eastern stations (b). The black dashed line indicates the circular mean, $\bar{\phi_f}$, of each dataset, with the grey-shaded region representing the circular standard error.

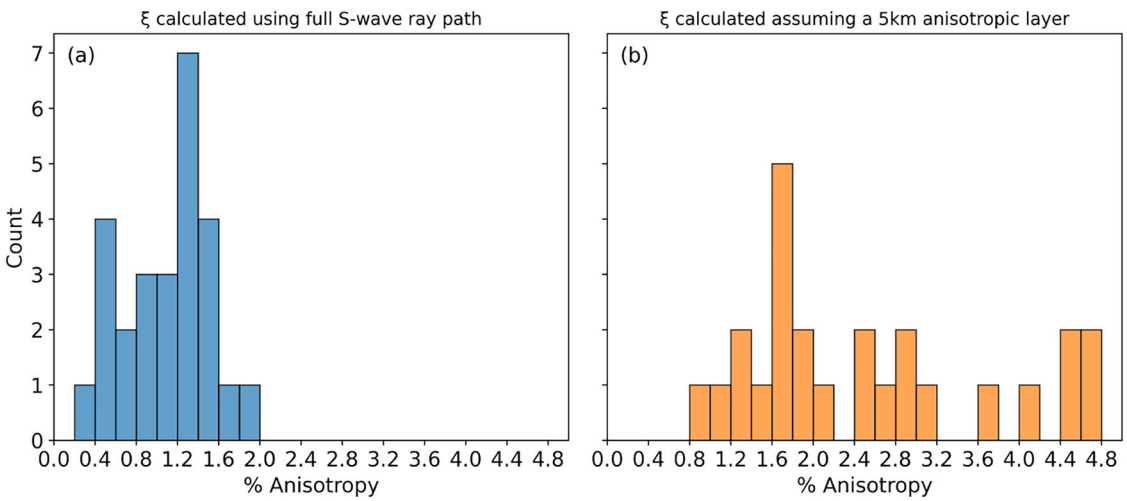

Figure 10 | Histograms showing the estimated percentage anisotropy, calculated following Equation (3), assuming that (a) anisotropy accumulates along the entire shear-wave ray-path and (b) anisotropy only in the uppermost 5 km of the crust. In (a), we assume a mean V_S of 5.7 km s^{-1} and in (b) we assume a mean V_S of 2.8 km s^{-1}.

manual inspection of all measurements unfeasible, requiring either robust automated data quality assurance or for input waveforms to be deghosted. Given that the effect of the seabed reflection on shear-wave polarisation is understood, it may be possible to construct deghosting operators as used for PS-waves using data recorded by PRM sensors (Gawron et al. 2025). Despite the potential interference from trench ghosts, trenching the sensors is still desirable given the reduction in RMS noise in the 5–30 Hz band (Bjerrum et al. 2014) as a low signal-to-noise ratio significantly increases shear-wave splitting measurement uncertainties (e.g., Restivo and Helffrich 1999; Michaud and Snieder 2004; Restivo and Helffrich 2006).

Presently, shear-wave splitting can be used to monitor S_{Hmax} azimuth using microseismicity (e.g., Igonin et al. 2022; Hudson et al. 2024; Kühn et al. Asplet et al. 2025) and to infer temporal variations in stress (e.g., Teanby, Kendall, Jones, et al. 2004; Stork et al. 2015). Further work should link models of stress-induced shear-wave splitting, such as the anisotropic poroelasticity model of Zatsepin and Crampin (1997), with geomechanical reservoir models. This would allow for the adaptation and extension of existing methods to invert shear-wave splitting for reservoir fractures (e.g., Verdon et al. 2009; Verdon and Kendall 2011; Al-Harrasi, Kendall, et al. 2011; Jones et al. 2014) or to resolve the magnitude of the in situ differential horizontal stress.

6 | Conclusion

If seafloor microseismic monitoring infrastructure is to be installed for offshore geological CO_2 storage projects, the information gained on the reservoir and surrounding formations should be maximised. We have shown, using analogous data from the permanent reservoir monitoring network at Snorre, that shear-wave splitting can be measured for microseismicity at the

field scale using seafloor instrumentation. Shear-wave splitting has the potential to enable monitoring of the in situ azimuth of maximum horizontal stress at a higher spatial resolution than borehole measurements and could be used for monitoring for fluctuations in maximum horizontal stress azimuth over time. At Snorre, we see that the measured shear-wave splitting fast polarisations are consistent with the regional maximum horizontal stress azimuth in the crust of 108 ± 4 with a possible 45° local rotation in maximum horizontal stress azimuth towards the south of the field. This variation may be due to the depletion history of the reservoir, similar to results at Valhall.

This work demonstrates that shear-wave splitting is a valuable tool for monitoring spatiotemporal changes in maximum horizontal stress azimuth, providing additional reservoir information at minimal added cost. The primary requirement is that the measurement of shear-wave splitting and the likely sources of microseismicity should be considered in the design and installation of the monitoring network. With further research to link geomechanical models and the geophysical observations, it may also be possible to use shear-wave splitting to constrain the magnitude of differential horizontal stress, further increasing the value of shear-wave splitting as a tool to monitor in situ stress for offshore CO_2 storage projects.

Acknowledgements

This work was conducted as part of the 'Stress history and reservoir pressure for improved quantification of CO_2 storage containment risks' (SHARP Storage) project, a collaboration between 16 research institutions and commercial companies in Norway, the United Kingdom, the Netherlands, Denmark, and India under the Accelerating CCS Technologies (ACT3) Programme. The SHARP project has been subsidised through ACT (EC Project no. 691712), by RCN and Gassnova (Norway), ROV (The Netherlands), DST (India), BEIS (UK) and EUDP (Denmark). We are grateful to Equinor ASA and license partners on Snorre (Harbour Energy Norge AS, INPEX Idemitsu Norge AS, Petoro AS, and Vår Energi ASA) for providing us with permanent reservoir monitoring system (PRM) data for the 21 March 2022 Tampen Spur event and its subsequent aftershocks. The views and opinions expressed in this research are those of the authors and are not necessarily shared by the license partners. TK was also supported by the University of Oxford's Strategic Research Fund through the Oxford Net Zero programme.

The authors thank Eirik Tvedt, Zoya Zarifi, Brian Baptie, Dan Roberts and members of the SHARP project for discussions, suggestions and feedback, which have improved and framed this work. We also thank two anonymous reviewers for their constructive feedback on this manuscript.

Part of this research was funded by the Natural Environment Research Council (NERC) [NE/W004976/1] as a part of the Agile initiative program at the Oxford Martin School.

Conflicts of Interest

The authors declare no conflicts of interest.

Data Availability Statement

The stress data used here is taken from the World Stress Map (Heidbach et al. 2025) and is publicly available. Earthquake detections and locations used here were first published by Jerkins et al. (2024), with picks being taken from the Norwegian National Seismic Network bulletin (Norwegian National Seismic Network (NNSN) 2025). The offshore waveform data was provided to us by Equinor, and the data are not openly accessible to the public. Figures were created using PyGMT (Uieda et al. 2021) and matplotlib (Hunter 2007). Preprocessing of waveform data was done using routines in Obspy (Beyreuther et al. 2010).

References

Al-Harrasi, O. H., A. Al-Anboori, A. Wüstefeld, and J.-M. Kendall. 2011. "Seismic Anisotropy in a Hydrocarbon Field Estimated From Microseismic Data." *Geophysical Prospecting* 59: 227–243. publisher: European Association of Geoscientists & Engineers. https://doi.org/10.1111/j.1365-2478.2010.00915.x.

Al-Harrasi, O. H., J. Kendall, and M. Chapman. 2011. "Fracture Characterization Using Frequency-Dependent Shear Wave Anisotropy Analysis of Microseismic Data." *Geophysical Journal International* 185: 1059–1070. https://doi.org/10.1111/j.1365-246x.2011.04997.x.

Asplet, J., M. Felgett, R. Luckett, J. Kendall, and D. Kühn. 2024. "*Seismic Anisotropy as a Measure of In-situ Stress for Safe* CO_2 *Storage." In the* 85th EAGE Annual Conference & Exhibition. European Association of Geoscientists & Engineers, vol. 2024, 1–5. https://doi.org/10.3997/2214-4609.2024101469.

Asplet, J., M. Fellgett, T. Kettlety, and J.-M. Kendall. 2025. "Passive Monitoring of *in situ* Stress Using Shear-Wave Splitting: Applications to CO_2 Storage and Beyond." Preprint, EarthArXiv, September 4. https://doi.org/10.31223/X5WT8S.

E Backus, G. 1962. "Long-Wave Elastic Anisotropy Produced by Horizontal Layering." *Journal of Geophysical Research* 67: 4427–4440. https://doi.org/10.1029/jz067i011p04427.

Baird, A. F., J.-M. Kendall, J. P. Verdon, et al. 2013. "Monitoring Increases in Fracture Connectivity During Hydraulic Stimulations From Temporal Variations in Shear Wave Splitting Polarization." *Geophysical Journal International* 195: 1120–1131. https://doi.org/10.1093/gji/ggt274.

Bauer, R. A., R. Will, G. El-Kaseeh, P. Jaques, S. Greenberg, and M. Carney. 2022. *Microseismic Monitoring, Event Location, and Focal Mechanisms at the Illinois Basin-Decatur Project, Decatur, Illinois*, USA American Geophysical Union (AGU), chap. 19, 321–341. https://doi.org/10.1002/9781119156871.ch19.

Beyreuther, M., R. Barsch, L. Krischer, T. Megies, Y. Behr, and J. Wassermann. 2010. "ObsPy: A Python Toolbox for Seismology." *Seismological Research Letters* 81: 530–533. https://doi.org/10.1785/gssrl.81.3.530.

Bjerrum, L., T. Matveeva, J. Lindgård, H. Rutledal, and A. Yde. 2014. "Comparison of Noise Characteristics on an Un-trenched and Trenched Cable Deployed in the North Sea for a PRM System." 2014, 1–5. https://doi.org/10.3997/2214-4609.20141050.

Booth, D. C., and S. Crampin. 1985. "Shear-Wave Polarizations on a Curved Wavefront at an Isotropic Free Surface." *Geophysical Journal International* 83: 31–45. https://doi.org/10.1111/j.1365-246X.1985.tb05154.x.

Cesca, S., F. Grigoli, S. Heimann, et al. 2014. "The 2013 September-October Seismic Sequence Offshore Spain: A Case of Seismicity Triggered by Gas Injection?." *Geophysical Journal International* 198: 941–953. https://doi.org/10.1093/gji/ggu172.

Chambers, K., J. Kendall, and O. Barkved. 2010. "Investigation of Induced Microseismicity at Valhall Using the Life of Field Seismic Array." *The Leading Edge* 29: 290–295. https://doi.org/10.1190/1.3353725.

Collins, J. A., C. J. Wolfe, and G. Laske. 2012. "Shear Wave Splitting at the Hawaiian Hot Spot From the PLUME Land and Ocean Bottom Seismometer Deployments." *Geochemistry, Geophysics, Geosystems* 13: _eprint. https://agupubs.onlinelibrary.wiley.com/doi/pdf/10.1029/2011GC003881.

Crampin, S. 1987. "Geological and Industrial Implications of Extensive-Dilatancy Anisotropy." *Nature* 328: 491–496. https://doi.org/10.1038/328491a0.

Dawson, A. F., M. Porter, and R. Frampton. 2016. "*Comparisons Between Buried and Laid Seabed Cable on the Valhall Field and Challenges in*

Processing PZ and PS Data." European Association of Geoscientists & Engineers, vol. 2016, 1–5. https://doi.org/10.3997/2214-4609.201601358.

De Meersman, K., J.-M. Kendall, and M. Van der Baan. 2009. "The 1998 Valhall Microseismic Data Set: An Integrated Study of Relocated Sources, Seismic Multiplets, and S-Wave Splitting." *Geophysics* 74: B183–B195. https://doi.org/10.1190/1.3205028.

Furre, A.-K., R. Meneguolo, P. Ringrose, and S. Kassold. 2019. "Building Confidence in CCS: From Sleipner to the Northern Lights Project." *First Break* 37: 81–87. https://doi.org/10.3997/1365-2397.n0038.

Gawron, M., P. Fallon, R. Haacke, et al. 2025. "4D PS-Wave Processing and Imaging With Trenched Sensors at the Snorre Field." In the *86th EAGE Annual Conference & Exhibition*., vol. 2025, 1–5. European Association of Geoscientists & Engineers. https://doi.org/10.3997/2214-4609.202510587.

Gerst, A., and M. K. Savage. 2004. "Seismic Anisotropy Beneath Ruapehu Volcano: A Possible Eruption Forecasting Tool." *Science* 306: 1543–1547. https://doi.org/10.1126/science.1103445.

Guzman, V., A. Li, and A. Savvaidis. 2022. "Stress Variations in the Delaware Basin From Shear-Wave Splitting Analysis." *Seismological Research Letters* 93: 3433–3443. https://doi.org/10.1785/0220220118.

Hall, S. A., and J.-M. Kendall. 2003. "Fracture Characterization at Valhall: Application of P-Wave Amplitude Variation With Offset and Azimuth (AVOA) Analysis to a 3D Ocean-Bottom Data Set." *Geophysics* 68: 1150–1160. https://doi.org/10.1190/1.1598107.

Harmon, N., D. W. Forsyth, K. M. Fischer, and S. C. Webb. 2004. "Variations in Shear-Wave Splitting in Young Pacific Seafloor."*Geophysical Research Letters* 31. _eprint. https://agupubs.onlinelibrary.wiley.com/doi/pdf/10.1029/2004GL020495.

Harvey, S., S. O'Brien, S. Minisini, S. Oates, and M. Braim. 2021. "Quest CCS Facility: Microseismic System Monitoring and Observations." In *Proceedings of the 15th Greenhouse Gas Control Technologies Conference*, 15–18. Elsevier. https://dx.doi.org/10.2139/ssrn.3817042.

Hatchell, P., P. Wills, and C. Didraga. 2009. "Production Induced Effects on Near-Surface Wave Velocities at Valhall." In the *71st EAGE Conference and Exhibition incorporating SPE EUROPEC 2009*, cp–127. European Association of Geoscientists & Engineers. https://doi.org/10.3997/2214-4609.201400331.

Heidbach, O., A. Barth, B. Müller, et al. 2016. "WSM Quality Ranking Scheme, Database Description and Analysis Guidelines for Stress Indicator." World Stress Map Technical Report 16-01. GFZ German Research Centre for Geosciences. https://doi.org/10.5880/WSM.2016.001.

Heidbach, O., M. Rajabi, D. Di Giacomo, et al. 2025. "*World Stress Map Database Release 2025*." GFZ Data Services. https://doi.org/10.5880/WSM.2025.001.

Herwanger, J. V., and S. A. Horne. 2009. "Linking Reservoir Geomechanics and Time-Lapse Seismics: Predicting Anisotropic Velocity Changes and Seismic Attributes." *Geophysics* 74: W13–W33,_eprint. https://pubs.geoscienceworld.org/seg/geophysics/article-pdf/74/4/W13/3220771/gsgpy_74_4_W13.pdf.

Hudson, T. S., T. Kettley, J.-M. Kendall, et al. 2024. "Seismic Node Arrays for Enhanced Understanding and Monitoring of Geothermal Systems." *The Seismic Record* 4: 161–171. https://doi.org/10.1785/0320240019.

Hunter, J. D. 2007. "Matplotlib: A 2D Graphics Environment." *Computing in Science & Engineering* 9: 90–95. https://doi.org/10.1109/MCSE.2007.55.

Igonin, N., J. P. Verdon, and D. W. Eaton. 2022. "Seismic Anisotropy Reveals Stress Changes Around a Fault as It Is Activated by Hydraulic Fracturing." *Seismological Research Letters* 93: 1737–1752. https://doi.org/10.1785/0220210282.

Jerkins, A. E., V. Oye, C. Alvizuri, F. Halpaap, and T. Kværna. 2024. "The 21 March 2022 Mw 5.1 Tampen Spur Earthquake North Sea: Location Moment Tensor and Context." *Bulletin of the Seismological Society of America* 114: 741–757. https://doi.org/10.1785/0120230163.

Jones, G., J.-M. Kendall, I. Bastow, D. Raymer, and A. Wuestefeld. 2014. "Characterization of Fractures and Faults: A Multi-Component Passive Microseismic Study From the Ekofisk Reservoir." *Geophysical Prospecting* 62: 779–796. https://onlinelibrary.wiley.com/doi/pdf/10.1111/1365-2478.12139.

Kendall, J.-M., Q. J. Fisher, S. C. Crump, et al. 2007. "Seismic Anisotropy As An Indicator of Reservoir Quality in Siliciclastic Rocks." In *Structurally Complex Reservoirs*, edited by S. J. Jolley, D. Barr, J. J. Walsh, and R. J. Knipe, Geological Society of London, Special Publication, vol. 292, 123–126. Geological Society of London. https://doi.org/10.1144/SP292.7.

Kendall, J-.M., T. Terakawa, M. Savage, et al. 2025. "Changes in Seismic Anisotropy at Ontake Volcano: A Tale of Two Eruptions." *Seismica* 4: 1101. https://doi.org/10.26443/seismica.v4i1.1101.

Keranen, K. M., and M. Weingarten. 2018. "Induced Seismicity." *Annual Review of Earth and Planetary Sciences* 46: 149–174. https://doi.org/10.1146/annurev-earth-082517-010054.

Kettley, T., D. Kühn, A. Jerkins, et al. 2025. "*North Sea Bulletin and Catalogue*." ISC Seismological Dataset Repository. https://doi.org/10.31905/5NSSO6OC.

Kettley, T., E. Martuganova, D. Kühn, et al. 2024. "A Unified Earthquake Catalogue for the North Sea to Derisk European CCS Operations." *First Break* 42: 31–36. https://doi.org/10.3997/1365-2397.fb2024036.

Kühn, D., A. M. Dichiarante, T. Kettley, et al. 2024. Stress field information from seismicity to de-risk large-scale CO2 injections in the North Sea Horda platform region. 363-363. Abstract from 39th General Assembly of the European Seismological Commission (ESC2024), Corfu, Greece.

Larsen, T. B., E. Skurtveit, S. Pearson, et al. 2025. SHARP project – an integrated approach for assessing CO2 storage containment risks. https://doi.org/10.5194/egusphere-egu24-5579.

Matcham, I., M. K. Savage, and K. R. Gledhill. 2000. "Distribution of Seismic Anisotropy in the Subduction Zone Beneath the Wellington Region, New Zealand." *Geophysical Journal International* 140: 1–10. https://doi.org/10.1046/j.1365-246x.2000.00928.x.

Michaud, G., and R. Snieder. 2004. "Error in Shear-Wave Polarization and Time Splitting." *Geophysical Prospecting* 52: 123–132. https://onlinelibrary.wiley.com/doi/pdf/10.1046/j.1365-2478.2003.00404.x.

Mordret, A., N. M. Shapiro, S. Singh, P. Roux, J.-P. Montagner, and O. I. Barkved. 2013. "Azimuthal Anisotropy at Valhall: The Helmholtz Equation Approach." *Geophysical Research Letters* 40: 2636–2641. https://agupubs.onlinelibrary.wiley.com/doi/pdf/10.1002/grl.50447.

Norwegian National Seismic Network (NNSN). 2025. "Earthquake Bulletin Data." Accessed July 25, 2025. https://doi.org/10.21348/b.0001.

Nowacki, A., M. Wilks, J. M. Kendall, J. Biggs, and A. Ayele. 2018. "Characterising Hydrothermal Fluid Pathways Beneath Aluto Volcano, Main Ethiopian Rift Using Shear Wave Splitting." *Journal of Volcanology and Geothermal Research* 356: 331–341. https://doi.org/10.1016/j.jvolgeores.2018.03.023.

Nur, A., and G. Simmons. 1969. "Stress-Induced Velocity Anisotropy in Rock: An Experimental Study." *Journal of Geophysical Research* 74: 6667–6674. https://doi.org/10.1029/JB074i027p06667.

Nuttli, O. 1961. "The Effect of the Earth's Surface on the S Wave Particle Motion." *Bulletin of the Seismological Society of America* 51: 237–246. https://doi.org/10.1785/BSSA0510020237.

Ottemöller, L., J. Michalek, J. Christensen, et al. 2021. "UiB-NORSAR EIDA Node: Integration of Seismological Data in Norway." *Seismological Research Letters* 92: 1491–1500. https://doi.org/10.1785/0220200369.

Pastori, M., P. Baccheschi, and L. Margheriti. 2019. "Shear Wave Splitting Evidence and Relations With Stress Field and Major Faults From the 'Amatrice-Visso-Norcia Seismic Sequence'." *Tectonics* 38: 3351–3372. https://doi.org/10.1029/2018TC005478.

Restivo, A., and G. Helffrich. 1999. "Teleseismic Shear Wave Splitting Measurements in Noisy Environments." *Geophysical Journal International* 137: 821–830. https://doi.org/10.1046/j.1365-246x.1999.00845.x.

Restivo, A., and G. Helffrich. 2006. "Core—Mantle Boundary Structure Investigated Using SKS and SKKS Polarization Anomalies." *Geophysical Journal International* 165: 288–302. https://doi.org/10.1111/j.1365-246X.2006.02901.x.

Savage, M. K., T. Ohminato, Y. Aoki, H. Tsuji, and S. M. Greve. 2010. "Stress Magnitude and Its Temporal Variation at Mt. Asama Volcano, Japan, from Seismic Anisotropy and GPS." *Earth and Planetary Science Letters* 290: 403–414. https://doi.org/10.1016/j.epsl.2009.12.037.

Scholz, J.-R., G. Barruol, F. R. Fontaine, et al. 2018. "SKS Splitting in the Western Indian Ocean From Land and Seafloor Seismometers: Plume Plate and Ridge Signatures." *Earth and Planetary Science Letters* 498: 169–184. https://doi.org/10.1016/j.epsl.2018.06.033.

Silver, P. G., and W. W. Chan. 1991. "Shear Wave Splitting and Subcontinental Mantle Deformation." *Journal of Geophysical Research* 96: 16429. https://doi.org/10.1029/91JB00899.

Skurtveit, E., D. Roberts, D. Kühn, et al. 2022. "Improved Quantification of CO_2 Storage Containment Risks—An Overview of the SHARP Storage Project." In the *16th Greenhouse Gas Control Technologies Conference 2022 (GHGT-16)*, Lyon, France, October 23–27, 2022. SSRN - Social Science Research Network.

Stork, A. L., J. P. Verdon, and J.-M. Kendall. 2015. "The Microseismic Response at the In Salah Carbon Capture and Storage (CCS) Site." *International Journal of Greenhouse Gas Control* 32: 159–171. https://doi.org/10.1016/j.ijggc.2014.11.014.

Teanby, N., J.-M. Kendall, R. H. Jones, and O. Barkved. 2004. "Stress-Induced Temporal Variations in Seismic Anisotropy Observed in Microseismic Data." *Geophysical Journal International* 156: 459–466. https://academic.oup.com/gji/article-pdf/156/3/459/5883127/156-3-459.pdf.

Teanby, N. A., J.-M. Kendall, and M. Van der Baan. 2004. "Automation of Shear-Wave Splitting Measurements Using Cluster Analysis." *Bulletin of the Seismological Society of America* 94: 453–463. https://doi.org/10.1785/0120030123.

Thompson, M., M. Andersen, R. Elde, S. Roy, and S. Skogland. 2015. "Delivering Permanent Reservoir Monitoring for Snorre and Grane." In the *Third EAGE Workshop on Permanent Reservoir Monitoring 2015*, vol. 2015, 1–5. European Association of Geoscientists & Engineers. https://doi.org/10.3997/2214-4609.201411980.

Uchida, N., J. Nakajima, K. Wang, et al. 2020. "Stagnant Forearc Mantle Wedge Inferred From Mapping of Shear-Wave Anisotropy Using S-Net Seafloor Seismometers." *Nature Communications* 11: 5676. https://doi.org/10.1038/s41467-020-19541-y.

Uieda, L., D. Tian, W. J. Leong, et al. 2021. "PyGMT: A Python Interface for the Generic Mapping Tools." *The Journal of Open Source Software* 6: 3488.

Verdon, J. P., and J.-M. Kendall. 2011. "Detection of Multiple Fracture Sets Using Observations of Shear-Wave Splitting in Microseismic Data." *Geophysical Prospecting* 59: 593–608. https://doi.org/10.1111/j.1365-2478.2010.00943.x.

Verdon, J. P., J.-M. Kendall, and A. Wüstefeld. 2009. "Imaging Fractures and Sedimentary Fabrics Using Shear Wave Splitting Measurements Made on Passive Seismic Data." *Geophysical Journal International* 179: 1245–1254. https://doi.org/10.1111/j.1365-246X.2009.04347.x.

Walsh, E., R. Arnold, and M. K. Savage. 2013a. "Silver and Chan Revisited." *Journal of Geophysical Research: Solid Earth* 118: 5500–5515. https://doi.org/10.1002/jgrb.50386.

Walsh, E., R. Arnold, and M. K. Savage. 2013b. "Silver and Chan Revisited." *Journal of Geophysical Research: Solid Earth* 118: 5500–5515. https://doi.org/10.1002/jgrb.50386.

Wuestefeld, A., O. Al-Harrasi, J. P. Verdon, J. Wookey, and J. M. Kendall. 2010. "A Strategy for Automated Analysis of Passive Microseismic Data to Image Seismic Anisotropy and Fracture Characteristics." *Geophysical Prospecting* 58: 755–773. https://doi.org/10.1111/j.1365-2478.2010.00891.x.

Zatsepin, S. V., and S. Crampin. 1997. "Modelling the Compliance of Crustal Rock-I. Response of Shear-Wave Splitting to Differential Stress." *Geophysical Journal International* 129: 477–494. https://doi.org/10.1111/j.1365-246x.1997.tb04488.x.